HHS Public Access

Author manuscript

*J Mol Cell Cardiol*. Author manuscript; available in PMC 2023 April 01.

Published in final edited form as:

*J Mol Cell Cardiol*. 2022 April ; 165: 115–129. doi:10.1016/j.yjmcc.2022.01.004.

# RBM20$^{S639G}$ mutation is a high genetic risk factor for premature death through RNA-protein condensates

**Chunyan Wang**[1], **Yanghai Zhang**[1], **Mei Methawasin**[2], **Camila Urbano Braz**[1], **Jeffrey Gao-Hu**[1], **Betty Yang**[1], **Joshua Strom**[2], **Jochen Gohlke**[2], **Timothy Hacker**[3], **Hasan Khatib**[1], **Henk Granzier**[2], **Wei Guo**[1,*]

[1]Department of Animal and Dairy Sciences, University of Wisconsin-Madison, WI 53706, USA

[2]Department of Cellular and Molecular Medicine, University of Arizona, Tucson, AZ 85724, USA

[3]Division of Cardiovascular Medicine, Department of Medicine, University of Wisconsin School of Medicine and Public Health, Madison, WI 53706, USA

## Abstract

Dilated cardiomyopathy (DCM) is a heritable and genetically heterogenous disease often idiopathic and a leading cause of heart failure with high morbidity and mortality. DCM caused by RNA binding motif protein 20 (RBM20) mutations is diverse and needs a more complete mechanistic understanding. RBM20 mutation S637G (S639G in mice) is linked to severe DCM and early death in human patients. In this study, we generated a RBM20 S639G mutation knock-in (KI) mouse model to validate the function of S639G mutation and examine the underlying mechanisms. KI mice exhibited severe DCM and premature death with a ~50% mortality in two months old homozygous (HM) mice. KI mice had enlarged atria and increased ANP and BNP biomarkers. The S639G mutation promoted RBM20 trafficking and ribonucleoprotein (RNP) granules in the sarcoplasm. RNA Seq data revealed differentially expressed and spliced genes were associated with arrhythmia, cardiomyopathy, and sudden death. KI mice also showed a reduction of diastolic stiffness and impaired contractility at both the left ventricular (LV) chamber and cardiomyocyte levels. Our results indicate that the RBM20 S639G mutation leads to RNP granules causing severe heart failure and early death and this finding strengthens the novel concept that RBM20 cardiomyopathy is a RNP granule disease.

## Graphical Abstract

*Correspondence should be directed to: Wei Guo, 1933 Observatory Dr., Rm 2112 Meat Science & Animal Biologics Discovery Building, Madison, WI 53706, USA. Tel.: +1 608-239-4375; wguo2@wisc.edu.

Author contributions

W. Guo, H. Granzier, M. Methawasin, T. Hacker, C.Y. Wang, Y.H. Zhang designed the experiments; C.Y. Wang, Y.H. Zhang, M. Methawasin, J. Gao-Hu, B. Yang, J. Strom, T. Hacker performed the experiments; C.Y. Wang, Y.H. Zhang, M. Methawasin, J. Strom, T. Hacker performed the animal study and tissue collections; C.Y. Wang, Y.H. Zhang, M. Methawasin, J. Strom, T. Hacker, C.U. Braz analyzed and interpreted the data; J. Gohlke performed motif analysis; C.Y. Wang and W.Guo wrote the paper; H. Granzier, M. Methawasin, T. Hacker, H. Khatib, Y.H. Zhang, C.U. Braz, J. Strom revised the paper.

**Conflict of interest**: None

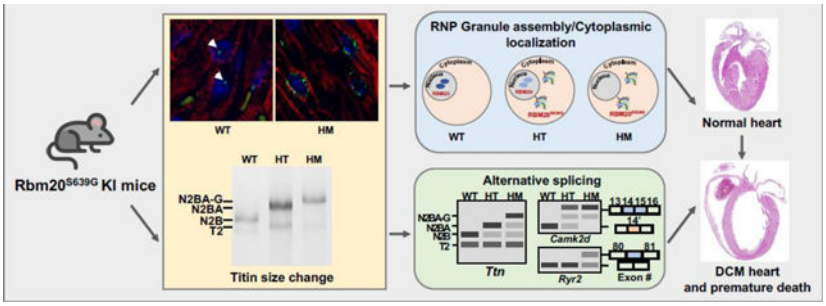


**Keywords**

RBM20 mutation; protein condensates; RNP granules; cardiomyopathy; heart failure; premature death

## Introduction

RNA binding motif protein 20 (RBM20) is an RNA binding protein and a splicing factor that is highly expressed in heart muscle [1, 2]. Genetic linkage analysis in human patients with dilated cardiomyopathy (DCM) identified mutations in *Rbm20* in ~3% of idiopathic DCM patients [1, 3]. These findings have placed *Rbm20* on the list of DCM-causing genes. DCM induced by RBM20 is now referred to as RBM20 cardiomyopathy. Loss-of-function studies using RBM20 knockout (KO) rats and mice revealed changes in splicing variants in over 30 genes including the myofilament gene *TTN* and calcium handling genes [2, 4–6]. Furthermore, complete depletion of RBM20 in rats and mice results in the development of DCM [2, 7]. Our recent study showed that adult *Rbm20* KO rats develop a DCM-like phenotype at about 6-month-old [8]. However, deletion of only the RNA binding motif (RRM) domain did not lead to an overt DCM-like phenotype even though the mice with RRM deletion manifested reduced Frank-Starling Mechanism, and an increase in fibrosis [5]. The underlying mechanisms by which complete RBM20 depletion results in DCM in rats and mice are widely accepted to be mainly associated with 1) reduced diastolic stiffness through alternative splicing of *TTN*, encoding the giant myofilament protein titin that is responsible for ventricular wall stiffness, and 2) impaired cardiomyocyte contractility through alternative splicing of calcium handling genes such as *Ryr2* and *Camk2d* [2, 4–6]. RBM20 depletion in rats leads to sudden death in about 17% of adult rats [2].

Recently, a *Rbm20* mutation knock-in (KI) ($Rbm20^{R636S}$) pig model [9] and a KI mouse model ($Rbm20^{S637A}$) [10] were generated revealing that pigs develop severe DCM and fatal circulatory failure in the majority of neonatal homozygous pigs [9] and atrial fibrillation and arrythmias in mutated mice [10]. These findings are consistent with human genetic studies showing that *Rbm20* mutations are associated with young age, end-stage heart failure and high mortality [1, 3, 11–17]. They also reported that the $Rbm20^{R636S}$ and $Rbm20^{S637A}$ mutations facilitated RBM20 re-localization from the nucleus to the cytoplasm and assembly of ribonucleoprotein (RNP) granules. These findings suggest that beyond gene splicing, RNP granules might also be responsible for severe DCM and early death by *Rbm20* mutations. A search of the National Center for Biotechnology Information ClinVar

database (https://www.ncbi.nlm.nih.gov/clinvar) using gene symbol *Rbm20*, reveals over 900 *Rbm20* mutations in need of functional validation. Two validated mutations in pig and mouse models are located in the highly conserved arginine/serine (RS)-rich domain, suggesting mutations in the RS domain seem relevant to RBM20 function.

In this study, we chose another uncharacterized mutation S639G in the RS region found in human patients to study whether this mutation is pathogenic. We generated an RBM20$^{S639G}$ mutation KI mouse model and examined the functional effects of the RBM20$^{S639G}$ mutation. Immunofluorescent staining in both paraffin-embedded tissues and isolated single cardiomyocytes was performed to determine protein trafficking and condensates. Transcriptomic profiling with deep RNA sequencing was carried out to identify genes with altered expression and splicing. Our results expand the functional validation of *Rbm20* mutations and further strengthens the novel concept that RBM20 cardiomyopathy is a protein condensate disease.

## Results

### RBM20$^{S639G}$ knock-in (KI) mice display enlarged heart chambers and thinner ventricular walls at an early age.

*Rbm20*$^{S639G}$ mutant KI mice were generated through CRSPR/Cas9 gene-editing technology. Sanger sequencing established the successful mutation at amino acid S639 and PCR confirmed the genotypes (Figure 1A). Both heterozygous (HT) and homozygous (HM) *Rbm20*$^{S639G}$ breeders yielded an average litter size (6–10) that follow Mendelian genetics. Gross anatomy demonstrated that HT and HM hearts had thin myocardial walls and were flabby, flimsy and distinctive from healthy wild type (WT) mice (Figure 1B). The whole heart of HT and HM mice could not maintain a sphere-like shape, a phenomenon noted in two months old male and female mice (Figure 1B). Histological assessments with hematoxylin and eosin (H&E) (Figure 1C) and Masson's trichrome staining (Figure 1D) revealed that both HT and HM mice displayed a DCM-like phenotype presenting as enlarged left ventricular chamber and thinner ventricular wall in two-month-old male and female mice. HM mice exhibited a more severe DCM-like phenotype (Figure 1C and 1D). However, histological analyses failed to reveal cardiac fibrosis in both HT and HM mice, as assessed by Masson's trichrome staining (Suppl Figure S1A and S1B). To test whether the mutation affects the expression of RBM20 level, we performed western blotting and the results showed that the protein expression levels of RBM20 were significantly elevated in both HT and HM mice with further increase in HM mice (Figure 1E).

### Functional assessment in RBM20$^{S639G}$ mutation KI mice.

Impaired cardiac function can cause and exacerbate atrial fibrillation (AF) and arrhythmia, and lead to heart failure. To assess the cardiac function of the *Rbm20* mutant KI mice, we performed both conscious and unconscious echocardiography in two months old mice. Electrocardiogram (ECG) recording was performed in combination with unconscious echocardiography. From the M-mode image analysis, both HT and HM survivors under unconscious conditions showed lower left ventricular (LV) ejection fraction (%EF) compared to WT mice in both genders (WT female, 40.4 ± 1.7%, WT male, 39.0 ± 2.1%;

HT female 19.6 ± 1.9%, HT male, 20.0 ± 1.8%; HM female, 19.4 ± 3.3%, HM male, 28.1 ± 1.4%) (Figure 2A). Left ventricular end diastolic diameter (LVDd) and systolic diameter (LVDs) were significantly larger in HT and HM survivors than WT mice in both males and females (Figure 2B and 2C). Similarly, fractional shortening (%FS) and relative wall thickness (RWT) of the LV (2*LVPW/LVDd), were decreased significantly in HT and HM mice compared to control mice (Suppl Table S2 and Figure 2D). We also observed a difference in LV diastolic parameters, such as mitral E/A ratios (the ratio of blood velocity through the mitral valve in early diastole (the E wave) to blood velocity in late diastole caused by atrial contraction (the A wave)) between genotypes and genders (Suppl Table S2). The mitral E/A ratio increased in the female HT mice; however, the ratio decreased in males HT compared to WT individuals (Figure 2E). E/E' (correlates LV filling pressure) was significantly elevated in the female HT mice but was normal in the males when compared to WT (Suppl Table S2). Increased filling pressure is one cause of LA hypertrophy and dilation, and this is consistent with the increase in LA dimensions found in HM females but not in males (Suppl Table S2). There were no major differences in right ventricular parameters, except RV internal diameter at systole (RVIDs) in females HM. Similarly, tricuspid annular plane systolic excursion (TAPSE), used as a parameter of global RV function, was only decreased in females (Suppl Table S2). In conscious echo, we found similar changes, such as increased LVDs, decreased %EF and %FS (Suppl Table S2) of HT mice both in females and males. In addition, the pressure-volume loop (PV-loop) analysis demonstrated a decreased %EF and increased end-systolic volume (ESV) and end-diastolic volume (EDV), indicating a dilated LV chamber, which is consistent with echocardiography data. We also observed that the HT mice had an increased potential energy (PE), decreased efficiency (Eff) and reduced maximum derivative of pressure (dP/dtmax) (Suppl Table S2). These data suggest that the RBM20$^{S639G}$ KI mice present a DCM phenotype, with enlarged LV chamber dimensions, decreased RWT, and reduced systolic function, with the severity and presentation differing between males and females.

### RBM20$^{S639G}$ mutation leads to altered gene expression linked to cardiac dysfunction.

We next performed transcriptomic profiling with deep RNA-sequencing (RNA Seq) to determine differentially expressed genes (DEGs) in RBM20$^{S639G}$ KI male mice. As expected, HM LVs had the highest number of DEGs when compared to HT and WT (2302 DEGs in HM vs. WT, 1168 DEGs in HM vs. HT, 597 DEGs in HT vs. WT) (Suppl Figure S2A and S2B). The higher number of DEGs in HM mice is consistent with their more severe phenotype. Gene enrichment analysis based on Human Phenotype Ontology (HPO) terms indicated that DEGs were related to cardiac dysfunction including DCM, abnormal LV function, hypertrophic cardiomyopathy, and left atrial enlargement (Figure 2F, Suppl Table S3). These findings are consistent with the above described gross anatomical, histological, and echocardiographic results. DEGs involved in ten cardiac pathology GO terms and three KEGG terms were indicated in the gene network and heatmap (Suppl Figure S2C through S2F, and S3A through S3D). Top 15 up- or down- regulated DEGs were illustrated by gene heatmap (Figure 2G) and eight of them (*Ankrd1*, *Ccn2*, *Enpp1*, *Lox*, *Fah*, *Slc40a1*, *Wnt5a*, and *Ryr1)* were validated with qPCR (Figure 2H). The results are consistent with RNA-seq data illustrated in the heatmap (Figure 2G). Many of these genes have previously been linked to cardiac dysfunction [18–26].

### RBM20$^{S639G}$ mutation caused early death in HM mice.

The survival rate was calculated by Kaplan–Meier estimator (Figure 3A). The survival rate in HM mice between one- to two-month-old was about 52% with no significant sex difference. Only 3% of HT mice died within two months, and no deaths occurred in WT mice. Two-month-old HM mice had significantly increased heart to body weight ratio (Figure 3B). Enlarged atria were observed only in HM mice (23.1% of total cases) (Figure 3C). Most interestingly, autopsy of HM mice with premature death revealed that LA/RA contained white and solid fat-like deposition and histological staining demonstrated that all mice had enlarged atria (Figure 3D). We also observed that HT and HM individuals developed abnormal heart rhythm with irregular PR and RR intervals from the ECG recordings during echocardiographic imaging (Figure 3E). In particular, the morphology of P wave suggests aberrant atrial conduction. RNA seq data showed that both natriuretic peptide precursor A (*Nppa*) and B (*Nppb*) were upregulated in HM individuals, and this was validated with qPCR (Figure 3F). Natriuretic peptides (ANP and BNP) are considered predictors of AF [27].

Further, gene enrichment analysis categorized the DEGs into ten arrhythmia related HPO terms and six abnormal conduction HPO terms representing 123 and 58 DEGs, respectively (Figure 3G, S4A, S4B, S4C, and 3J, S4D, S4E, S4F). The top 15 up- or down-regulated DEGs from these GO terms were clustered in gene heatmaps (Figure 3H and 3K). These data further support the observations of early premature death that is associated with malignant arrhythmia in KI mice. Genes selected from the top 15 up- or- down-regulated DEGs were validated through qPCR (Figure 3I and 3L).

### RBM20$^{S639G}$ mutation facilitates trafficking of RBM20 from the nucleus to the sarcoplasm with formation of protein condensates in the sarcoplasm.

Previous studies, including ours, have shown that a single amino acid substitution in the RS rich domain of RBM20 causes severe DCM [1–3]. However, it is unclear how a single amino acid substitution results in cardiac remodeling and pathogenesis. In neurodegenerative disease, mutated RNA binding proteins can assemble into ribonucleoprotein granules (RNP) or RNA-protein condensates [28, 29], which is the primary cause for pathogenesis. To test if this might also occur in heart muscle disease, immunofluorescent staining in both paraffin-embedded tissues and in isolated single cardiomyocyte was performed. This demonstrated formation of protein condensates at the nuclear periphery or nuclear membrane, whereas unmutated RBM20 was constrained in the nucleus where it forms protein condensates providing evidence that the S639G amino acid substitution facilitates RBM20 trafficking from the nucleus to the sarcoplasm (Figure 4A and 4B, Suppl Figure S9, Suppl Video 1 and 2). The RNP is assembled from mRNA transcripts and proteins, most of which are RNA binding proteins (RBPs) or RNA chaperones; a diverse number of intermolecular interactions involving potential RNA–protein, protein–protein, and RNA–RNA interactions play a key role in RNP congregation [30, 31], trapping both RNAs and RBPs in the cytoplasm. The GO enrichment analysis of DEGs (WT vs. HT vs. HM) for both Molecular Function and Biological Process from RNA-Seq data validated that GO terms associated with protein binding and regulation of localization have relatively lower *P*-values compared to other GO terms (Figure 4C, Suppl Tables S4 and S5). Besides,

differentially alternative spliced (DAS) genes were mostly clustered in the GO terms (cellular component and biological process) related to intracellular organelle, organelle and cellular component organization (Suppl Figure S5). Taken together, these data suggest that the RBM20$^{S639G}$ mutation may create the cellular and molecular microenvironment for RNA-protein assembly and condensation.

Considering that the formation of RNA-protein condensates is likely to disturb the process of mRNA translation, we examined the expression of genes that are involved in translational regulation and the previously reported components of stress granules [32–38], one category of RNP aggregates. We found that the components of stress granules were dysregulated in RBM20$^{S639G}$ mice when compared to WT (Figure 4D), and genes associated with translational regulation were also differentially expressed in RBM20$^{S639G}$ mice (Figure 4E). For instance, eukaryotic translation initiation factor 4E (eIF4E, *Eif4e*), which plays a critical role in the control of cap-dependent translation initiation [39, 40], was found decreased in brain ischemia induced formation of stress granule [41]. Meanwhile, eIF4E is an RNP component [37, 38] that also regulates the fate of RNP granule formation through multiple mechanisms [42]. Further, *Hsp90aa1*, encoding the human stress-inducible 90-kDa heat shock protein alpha (Hsp90A), is involved in the formation of RNP granules [43–45]. Both proteins were differentially expressed in the RBM20$^{S639G}$ mice (Figure 4D and 4E). We further did co-staining of RBM20 and stress granule core proteins, such as G3BP1, TIA-1/TIAR in isolated cardiomyocytes. We did not observe the colocalization of RBM20 and stress granule markers. However, induced stress granules in sodium arsenite-treated RBM20$^{R636S}$ mutation-transfected U2OS cells colocalized mutated RBM20 and stress granule markers (9), suggesting the RBM20 mutation-induced RNP granules do not completely share the same components within the stress granules (Suppl Figure S7).

## RBM20$^{S639G}$ mutation regulates mRNA posttranscriptional process.

We have reported that loss-of-function mutations in RBM20 (depletion of RBM20 in cardiomyocytes) in rats results in the expression of larger titin isoforms, due to splicing deficiency of the titin (*TTN)* gene [2]. Re-localization of RBM20 at the nuclear periphery caused by *Rbm20* mutation reduces the level of RBM20 in the nucleus, suggesting that *Rbm20$^{S639G}$* mutation could interfere with the mRNA posttranscriptional process, similarly to RBM20 depletion. To test this, we studied titin isoform expression using agarose gel electrophoresis. As expected, we observed large titin isoforms in HT and HM hearts similar to RBM20 KO hearts (Figure 5A). Further, splicing analysis with RNA-seq data revealed that 145 genes were differentially spliced in HT and 162 genes in HM mutated hearts (Suppl Figure S6A and Tables S6, S7). The volcano and violin plots showed the pattern of the differentially alternative spliced (DAS) genes in HT or HM with five alternative splicing events (SE, skipped exon; A5SS, alternative 5’ splice site; A3SS, alternative 3’ splice site; MXE, mutually exclusive exons; RI, retained intron) (Figure 5B and 5C). The SE event was the most frequent event of DAS genes (Figure 5B and 5C). In addition to *TTN,* two alternatively spliced genes *Ryr2* and *Camk2d* in RBM20 KO rats and mice were also found differentially spliced in both HT and HM mutated hearts (Figure 5D, Suppl Figure S8, Suppl Tables S6, S7). In addition to those miss-spliced genes observed in RBM20 KO hearts, splice mismatches of additional genes were observed in *Rbm20* mutations (Suppl

Figure S6A and Tables S6, S7). Further, motif analysis showed that all 145 alternatively spliced HT genes and all 162 alternatively spliced HM genes contain potential RBM20 ("TCTT"/"UCUU") motifs, indicating interaction of RBM20 with the alternatively spliced genes (Suppl Tables S6, S7). Introns adjacent to the alternatively spliced exon ("intron upstream", "intron downstream") can be found in Table S9 by their isoform identifiers with positional information about RBM20 binding motifs. Six of these genes (*Phldb1, Tpm2, Ambra1, Epb41, Mtg2 and Ppox)* were validated by RT-PCR, which is consistent with the RNA-seq data (Figure 5D, Suppl Figure S8). HPO terms and GO terms of Cellular Component (CC) and Molecular Function (MF), and KEGG pathways of the DAS genes were summarized by Venn diagrams (Suppl Figure S6B through S6E). Gene enrichment analysis based on HPO indicated that DAS genes (HM vs. WT) were associated with atrial arrhythmia ($P = 9.46\times10^{-5}$), atrial fibrillation ($P = 9.46\times10^{-5}$), tachycardia ($P = 0.016$), and sudden death ($P = 0.021$) (Figure 5E and Suppl Table S8). The five alternative splicing events of the DAS genes representing the top 15 HP terms are shown here (Figure 5E).

## RBM20$^{S639G}$ mutation reduced cardiomyocyte diastolic stiffness and impaired cardiomyocyte contractility.

Titin plays a major role in diastolic function and ventricular filling [46]. Size switching of titin is one of the primary mechanisms modifying the elastic properties of titin and altering cardiomyocyte function [47–50]. To determine how RBM20$^{S639G}$ mutation alters cardiac function at the cellular level, we performed experiments in loaded and unloaded intact cardiomyocytes. Due to the higher mortality rate in HM mice, only HT mice were used in this study. In the loaded intact myocyte study, the cell was glued to the force transducer and the length controller. Single cell force measurements were performed using a work loop protocol, which is the cellular equivalent of pressure-volume (PV) loop analysis at the LV level [51]. The slopes of ED-SSLR (end diastolic stress sarcomere length relation) and ES-SSLR (end systolic stress-sarcomere length relation) which reflect the cellular diastolic stiffness and systolic contractility, respectively, were obtained (Figure 6A, 6B and 6C). Representative cellular work loops are shown in Figure 6A. Intact cardiomyocytes from HT had decreased ED-SSLR and ES-SSLR slopes, compared to WT myocytes (Figure 6B and 6C). The maximal rate of stress rise ($dS/dt_{max}$) during isometric contraction is reduced in HT (Figure 6D), but the maximal rate of stress decline ($dS/dt_{min}$) is not different from WT (Figure 6E). These results indicate reduced cellular diastolic stiffness due to expression of large titin isoforms, and systolic contractility in HT cardiomyocytes. In the unloaded intact myocyte, sarcomere length (SL) shortening and re-lengthening were evaluated. The baseline SL of HT myocytes were observed to be shorter than WT (Figure 6F). In contrast, the shortening amplitude was larger in HT (Figure 6G). Additionally, the time to peak shortening was prolonged while the time from peak to 50% baseline was unaltered (Figure 6H and 6I), consistent with the reduced $dS/dt_{max}$ and normal $dS/dt_{min}$ observed in loaded cells (Figure 6D and 6E). $Ca^{2+}$ transients were measured with Fura-2. There was no significant difference in diastolic baseline signal (Figure 6J), while the transient amplitude was larger in HT (Figure 6K). The time to peak transient was prolonged in HT mice (Figure 6L), while the time from peak to 50% decay was unaltered (Figure 6M). The delay in $Ca^{2+}$ release contributed to the reduced contraction velocity (Figure 6H and 6L). Overall,

the results demonstrate changes in $Ca^{2+}$ release kinetics and contractile dysfunction of HT myocytes.

## Discussion

Our findings show that RBM20$^{S639G}$ mutation results in severe DCM, atrial dysfunction, arrythmia and a high mortality rate in young mice. In addition, RBM20 S639G mutation promotes protein-RNA condensates in the sarcoplasm. These findings are consistent with observations in human genetic studies showing human subjects carrying RBM20 mutations suffer from severe heart failure and early death [1, 3, 11–17]. There are over 900 RBM20 mutations listed in the NCBI ClinVar database. Recently, two mutations (R636S and S637A) located in the RS domain have been validated in pig and mouse model respectively [9, 10]. Both gene-edited mutant KI pigs (RBM20$^{R636S}$) and mice (RBM20$^{S637A}$) display an accumulation of stress granule-like structures in the sarcoplasm. Homozygous piglets are more severely affected than heterozygous piglets. All neonatal homozygous piglets develop a moderate-to-severe DCM phenotype with poor growth and low survival rate [9]. *Rbm20*$^{S637A}$ mice also exhibit severe DCM phenotypes with a high prevalence of atrial fibrillation and ventricular tachycardia and an increased early death rate, mimicking the clinical observations in human patients carrying S637A mutation [10]. In the present study, we selected the S639G mutation that is also located in the RS domain. The *Rbm20*$^{S639G}$ KI mouse model demonstrated a phenotype similar to the RBM20$^{R636S}$ pig and RBM20$^{S637A}$ mouse models. Mice homozygous for RBM20$^{S639G}$ mutation exhibit ~50% mortality by ~2 months of age, which is even worse than that in *Rbm20*$^{S637A}$ mice. Our results further establish that mutations in the RS domain of RBM20 contribute to RBM20 cardiomyopathy. Mutations outside the RS domain may also cause RBM20 cardiomyopathies, whether this is indeed the case needs to be addressed in future studies.

A decade ago, RBM20 was identified as a regulator of the *TTN* gene alternative splicing, encoding the giant sarcomeric protein titin that is responsible for ventricular wall stiffness [2, 46] and 30 other genes including calcium handling genes [4, 6]. Subsequent studies using RBM20 KO rats and mice revealed that RBM20 loss-of-function leads to reduced diastolic stiffness, DCM phenotype, arrhythmia and sudden death [2, 5–7]. Therefore, it is widely accepted that RBM20 cardiomyopathy is caused by altered splicing variants of *TTN* and 30 more genes. Recent studies in RBM20 mutation KI animal models, including ours, indicated that RBM20 mutations lead to a cardiac phenotype similar to, but more severe than RBM20 KO, suggesting RBM20 mutations result in a gain-of-function. The new function gained from RBM20 mutations is associated with RBM20 re-localization and stress granule-like structure formation in the cytoplasm. Why do RBM20 mutations regulate splicing variants of the same genes as in RBM20 KO? RBM20 is a nuclear protein and when RBM20 is knocked out it would eliminate RBM20 from the entire cell, including the nucleus, resulting in abnormal posttranscriptional regulation. However, RBM20 mutations may facilitate RBM20 shuttling from the nucleus to the sarcoplasm, which depletes RBM20 from the nucleus and causes an accumulation in the sarcoplasm. This may explain why RBM20 mutated animals exhibit a similar cardiac phenotype as the RBM20 KO animals. Furthermore, protein condensates in the sarcoplasm promoted by RBM20 mutations may interrupt the translational process by trapping RNAs and proteins in the stress granule-

like structure, thereby changing the RNA concentration and intermolecular RNA-RNA interactions [31]. In addition, RNP granules are enriched with RNA binding proteins (RNPs) that may not be released to facilitate normal transcriptional and posttranscriptional regulation. Thus, these trapped RNPs interfere with these important biological processes [31, 52]. The alterations in transcriptional and post-transcriptional regulation may also explain why we found so many additional differentially expressed and spliced genes in hearts from mice with RBM20 mutations, and a severe phenotype such as atrial enlargement and high mortality at young age, compared to *Rbm20* KO rodent models.

Lastly, our results with RBM20$^{S639G}$ KI mice and recently published data with RBM20$^{R636S}$ pigs and RBM20$^{S637A}$ mice suggest that RBM20 mutations place patients at high risk for severe cardiac dysfunction and premature death. RNP granules caused by mutations in RNA binding proteins (RBPs) have been extensively studied in neurodegenerative diseases [53]. Mutations in the *TARDBP* gene, encoding the RNA binding protein TDP43 promote RNP granules in the neurons and result in neurodegenerative diseases [54, 55]. In this regard, RBM20 cardiomyopathy caused by RBM20 mutations might be analogous to RNP granule disease. Future studies on mechanisms of RBM20 trafficking and the formation of RNA-protein condensates in the sarcoplasm are warranted. Answers to these questions will allow us to develop therapeutic strategies to prevent or reverse DCM caused by RBM20 mutations. In addition, posttranslational modifications (PTMs) in the RS domain of RBPs are critical for posttranscriptional regulation and nucleocytoplasmic transportation [56, 57]. Our previous mass spectrometry study demonstrated that RBM20 is highly phosphorylated in the RS domain [58]. Hence, future studies should also address the role of PTMs in cardiac pathogenesis induced by RBM20 mutations.

## Methods

### Generation of *Rbm20*$^{S639G}$ mutation knock-in mice and tissue sample preparation

The *Rbm20*$^{S639G}$ mouse (BL6J) was generated via CRISP/Cas9 system at the Genetically Engineered Mouse Models Core Facility of the University of Arizona using the CRISPR/Cas9 system. The CRISPR guide RNAs (gRNAs), used for mouse *Rbm20*$^{S639G}$ knock-in were designed using the CRISPOR web tool (http://crispor.tefor.net/). The gRNAs CTCATTGGACTTCGAGAACGTGG (gRNA1) and CTTCGAGAACGTGGCCGCTCTGG (gRNA2) (PAM sequence was underlined) were designed for the CRISPR knock-in experiments. Oligos with 40–50 bp homology to sequences on each side of each gRNA-mediated double-stranded break were designed. The mixture of Cas9 protein with sgRNA complexes and oligo were injected into the pronucleus of 1-cell zygotes from the fertilized eggs collected from the oviducts of super ovulated BL6/NJ females. The genetically edited mice were identified by PCR genotyping, as well as Sanger sequencing. Two screening primers: forward, 5’- TGTGTGTCTCCATCTGGGTG and reverse, 5’-CTTTGTCCAGCTGCCTAGGA, producing 307 bp band for the wild type and two additional bands of 207bp and 100bp in the positive mice (heterozygous, HT) when restricted with *XhoI*.

Animals were maintained on standard rodent chow. Hearts were removed immediately after euthanasia and the left ventricle, right ventricle, and atria were separated. Samples were collected from 8-week-old mice. Tissues were separated for paraffin-embedding and snap-frozen in liquid nitrogen and stored in a −80°C freezer until use. All animal experiments were in accordance with the guidelines of the Care and Use of Laboratory Animals of the National Institutes of Health. The protocol was approved by the Institutional Animal Care and Use Committee (IACUC) of the University of Wisconsin-Madison (#A006262) and the University of Arizona (#09–056).

## Histological assessments

Whole hearts from two-months-old mice were isolated and fixed in 4% paraformaldehyde, paraffin-embedded, and stained with Hematoxylin and Eosin (H&E) (n=3), Masson's trichrome. Stained sections were photographed (BZ-X800, Keyence), and the fibrotic area was quantified by using ImageJ software (Fiji) [59]. The proportion of fibrotic area was calculated as a ratio of the fibrotic area to the total cross-sectional area.

**Immunochemistry staining and cell imaging—**Isolated cardiomyocytes were fixed with methanol for 15 min on ice and blocking/permeabilized with 10% goat serum (Sigma-Aldrich; Cat#: G6767), 0.2% Triton-X100 (Sigma-Aldrich; Cat#: X100) in TBS for 1 hour at room temperature (RT). Then cells were incubated with primary antibodies, rabbit anti-RBM20, CoraLite®594-conjugated G3BP1 Monoclonal antibody (Cat#: CL594–66486, Proteintech), TIA-1/TIAR (D-9) mouse mAb (Cat#: sc-48371, Santa Cruz Biotechnology), mouse monoclonal anti-alpha-actinin antibody (Cat#: A7811, Sigma-Aldrich), in blocking/permeabilized buffer for 1 hour at RT or overnight at 4°C. After washing, cells were spined down and incubated with Alexa flour-conjugated secondary antibody (Goat anti-rabbit, Alexa Fluor 488, Cat#: A32731, Invitrogen; Goat anti-mouse, Alexa Flour 594, Cat#: 8890, Cell Signaling Technology) for 1 hour at RT, washed with TBST, and mounted in SlowFade™ Gold Antifade Mountant with DAPI (Invitrogen; Cat#S36938). Cells were visualized using Keyence BZ-X800 microscope (Osaka, Japan).

The antibodies and procedure for the immunostaining of the paraffin embedded tissue is the same after deparaffinizing and rehydrating, permeabilization, and epitope retrieval.

**Western blotting and subcellular protein fractionation—**Total proteins were lysed from heart LV tissues as described previously [8]. Briefly, proteins were separated by SDS-PAGE gel and transferred onto a PVDF membrane. The membrane was probed with primary antibodies against RBM20 (1:1000, rabbit), GAPDH (1:1500, rabbit; Cell Signaling Technology, Danvers, Massachusetts, USA; Cat#2118S) was served as the protein loading control. Then the membrane was probed with horseradish peroxidase-coupled secondary antibodies (1:3000, anti-rabbit; Promega; Cat#W4011) for 1 hour. Chemiluminescence images were taken by ChemiDoc system (Bio-Rad, Hercules, CA).

Subcellular proteins were extracted from LV at two-months-old mice followed the instruction (Thermo Fisher Scientific, Waltham, MA; Cat# 87790). Cytoplasmic extract and nuclear extract were loaded into SDS-PAGE gel and transferred onto PVDF membrane. The membrane was probed with primary antibodies against RBM20, HSP90 (1:1000, rabbit; Cell

Signaling Technology, Danvers, Massachusetts, USA; Cat# #4874), GAPDH and Histone H3 (1:1500, rabbit; Cell Signaling Technology, Danvers, Massachusetts, USA; Cat# #4499). Incubation with secondary antibody and taken chemiluminescence images were descripted above.

## Echocardiography

To assess cardiac function *in vivo*, wild type (WT), heterozygous RBM20$^{S639G}$ mutant (HT), and homozygous RBM20$^{S639G}$ mutant (HM) male and female mice at the age of two months were used. Echocardiographic analysis has been done in two different laboratories independently. Transthoracic echocardiography was performed using a Visual Sonics Vevo 3100 ultrasonography outfitted with the MX400 transducer, ~30-MHz, as detailed previously [60]. To acquire of two-dimensional guided M-mode images at the tips of papillary muscles and Doppler studies, mice were sedated by facemask administration of 1% isoflurane, hair removed, and maintained on a heated platform. Blood velocities across the mitral, aortic and pulmonary valves were measured using Doppler pulse wave imaging angling the probe to obtain a nearly parallel orientation to the blood flow.

End diastolic and systolic left ventricular (LV) diameter and anterior and posterior wall (AW and PW, respectively) thickness were measured online from M-mode images obtained in a parasternal short-axis view using the leading edge-to-leading edge convention. All parameters were measured over at least three consecutive cardiac cycles and averaged. Left ventricular fractional shortening were calculated as [(LV diameter$_{diastole}$ −LV diameter$_{systole}$)/LV diameter$_{diastole}$] × 100; ejection fraction [(7.0/ (2.4 + LV diameter$_{diastole}$) (LV diameter$_{diastole}$)$^3$ − (7.0/ (2.4 + LV diameter$_{systole}$) (LV diameter$_{systole}$)$^3$/ (7.0/ (2.4 + LV diameter$_{diastole}$) (LV diameter$_{diastole}$)$^3$ × 100 and LV mass was calculated by using the formula [1.05 × ((Posterior Wall $_{diastole}$+Anterior Wall$_{diastole}$+LV diameter$_{diastole}$)$^3$ − (LV diameter$_{diastole}$)$^3$)]. Right ventricular wall thicknesses were measured as above from M-mode images obtained in a right parasternal long-axis window. Pulmonary artery (PA) diameter was measured just distal to the pulmonary valve. Care was taken to measure PA diameter during the widest part of the ejection cycle. The aortic diameter was measured just distal to the aortic valve. Heart rate was determined from at least three consecutive intervals from the pulse wave Doppler tracings of the LV outflow tract. Ejection time was measured from the same outflow track tracings from the onset of flow to the end of flow. Isovolumic relaxation time was measured as the time from the closing of the aortic valve to the opening of the mitral valve from pulse wave Doppler tracings of the LV outflow tract and mitral inflow region. All images and measures were obtained by the same observer.

Mice were anesthetized under 1–3% isoflurane (USP, Phoenix) in oxygen mixture, then placed in dorsal recumbence on a heated platform for echocardiography. Transthoracic echo images were obtained with a Vevo 3100 High Resolution Imaging System (Visual-Sonics, Toronto, Canada) using the model Mx550D scan head designed for murine cardiac imaging. Body temperature was maintained at 37°C. Imaging was performed at a depth setting of 1 cm. Images were collected and stored as a digital cine loop for off-line calculations. Standard imaging planes, M-mode, Doppler, and functional calculations were obtained according to American Society of Echocardiography guidelines. The parasternal long-axis

view and mid-wall cross sectional view of the left ventricle (LV) were used to calculate percentage fractional shortening, percentage ejection fraction, and ventricular dimensions and volumes. In addition, the left atrial dimension was measured in the short-axis view directly below the aortic valve leaflets. LV filling parameters (E and A wave, E' and A', and deceleration time) were acquired from the images of mitral valve Doppler flow or mitral annulus tissue Doppler from an apical view. A sweep speed of 100 mm/sec was used for M-mode and Doppler studies. The heart rate of animals during echocardiographic study were maintained in the range of 500 −550 beats/min for M-mode, 500– 550 beats/min for B-mode and 400 to 500 beats/min for Doppler studies.

Conscious echocardiography was performed in animals restrained through scruffing the skin at the nape of the neck. Short axis M-mode cine loops at the level of the mid-papillary were recorded for evaluation of morphometry and systolic LV function, as described in the anesthetized echocardiography.

## Pressure-Volume analysis

*In vivo* pressure volume analysis was performed using a SciSense Advantage Admittance Derived Volume Measurement System and 1.2F catheters with 4.5 mm electrode spacing (SciSense, London, Ontario, Canada). Mice were anesthetized and ventilated with 1–3% isoflurane using an SAR-1000 Ventilator (CWE Inc) and body temperature maintained at 37°C using a MouseMonitor S platform (Indus Instruments). Mice were secured and the abdomen was opened below the sternum. The apex of the LV was punctured using a 28G needle and the catheter was advanced into the LV. The IVC was located and occluded during a pause in ventilation to acquire load-independent indexes. Data acquisition and analysis was performed in LabScribe3 (iWorx, Dover NH). The end-systolic pressure-volume relationship was fit to a linear equation ($P = E_{es} \cdot V + b$). The end-diastolic pressure-volume relationship was analyzed using a monoexponential fit ($P = Ae^{\beta V} + C$) with the exponent (β) reported as the stiffness.

## Adult mouse intact cardiomyocyte isolation

Cardiomyocytes were isolated as described previously [61]. Briefly, mice were anesthetized under isoflurane. The heart was removed and cannulated via the aorta with a blunted 21-gauge needle for antegrade coronary perfusion. The heart was perfused for 4 min with perfusion buffer ([in mmol/L] 90 NaCl, 34.7 KCl, 0.6 KH2PO4,0.6 Na2HPO4, 1.2 MgSO4, 12 NaHCO3, 10 KHCO3, 10 HEPES, 10 taurine, 5.5 glucose, 5 BDM, 20 creatine, pH 7.4), followed by digestion buffer (perfusion buffer plus 0.05 mg/ml Liberase TM research grade; Roche Applied Science, and 13 μM CaCl2) for 20 min. Then, the heart was placed in myocyte stopping buffer (perfusion buffer plus bovine calf serum 0.08 [BCS]/ml and 8 μM CaCl2) with protease inhibitors ([in mmol/L] 0.4 Leupeptin, 0.1 E64, and 0.5 PMSF (Peptides International, Sigma-Aldrich)). The left ventricle was cut into small pieces and triturated several times with a transfer pipette and then filtered through a 100 μm nylon mesh filter. Then $Ca^{2+}$ was reintroduced to cardiomyocyte suspension to a final concentration of 1 mM.

## Cellular work loop force measurement

All intact cell experiments were performed at temperature 37°C in Medium199 (M5017, Sigma-Aldrich) plus 10 μg/mL insulin (I9278, Sigma-Aldrich). Cells were field stimulated at 4 Hz frequency by MyoPacer stimulator (IonOptix Co, MA). An inverted microscope (IX-70; Olympus) was used with a chamber that had platinum electrodes to electrically stimulate cells and a perfusion line with heater control and suction out to maintain a flow rate of 2 ml/min. All images were recorded with 40X objective lens. Data were collected using an IonOptix FSI A/D board and IonWizard 6.3 software (IonOptix Co, MA) with SarcLen and SoftEdge modules to determine sarcomere length (SL) and cell width. The sampling frequency of the system was sufficient to measure force (1,000 Hz) and SL (250 Hz) simultaneously. The myocyte was glued with Myotak (IonOptix LLC) at one end to a glass rod that attached to the force transducer (OFT200, OptiForce transducer, IonOptix LLC) and the other end to a glass rod that attached to the piezo translator (Mad City Lab). Cross sectional area of intact cell was obtained from the measured cell width assuming that the cross section of the cell was an ellipse [62]. All forces were normalized to stress.

The cell work loop algorithm was applied through the interface box of the IonOptix system which contains a field programable gate array (FPGA) that digitizes the force signal, and the preload and after load value programmed through the IonWizard software 6.3, as described in [63]. The output from the FPGA drove the piezo translator to adjust cell length through a feedback control system based on developed force, implementing preload and afterload. The system constructs force-SL loops by modulating cell length, generating 4 phases that mimic isovolumic contraction, systolic ejection, isovolumic relaxation and diastolic filling phases of the LV chamber[20]. Data analysis was performed in LabScribe3 (iWorx, Dover, NH). The ED-SSLR (end diastolic stress-sarcomere length relation) and ES-SSLR (the end systolic stress-sarcomere length relation) were fit with linear relation.

## Unloaded intact cardiomyocytes

Measurement of $Ca^{2+}$ release-reuptake and SL shortening-relengthening in unloaded intact cardiomyocytes was performed as follows. Isolated LV cardiac myocytes were incubated with 1 uM Fura-2 AM (F-1225, Life Technologies). Fluorescence was measured ratiometrically with the IonOptix photometry MultiCell High Throughput system (IonOptix Co, MA). Fura-2 was excited alternately at 340 and 380 nm, and emission was recorded at 510 nm. Background fluorescence was subtracted for each excitation wavelength. Ratio of fluorescence intensities excited at 340 nm and 380 nm was used as a relative measurement of cytoplasmic $Ca^{2+}$, the ratio transient was fitted by monotonic transient analysis software (IonWizard Transient Analysis Tool 1.2.97.0). All measurements were carried out at 37°C. The SL shortening-relengthening was measured in cells that were not loaded with Fura-2.

## Titin gel electrophoresis

Titin isoforms were resolved by a previously published method using a vertical sodium dodecyl sulfate (SDS)-1% agarose gel electrophoresis (VAGE) system [64, 65]. The frozen left ventricle samples from 2-month-old mice were homogenized in urea-thiourea-SDS-dithiothreitol sample buffer using a small Dounce homogenizer or Geno/Grinder (SPEX SamplePrep, Metuchen, NJ) at 1500 strokes/min for 1 min, repeat for 5–7cycles and were

heated at 65°C for 10 min. The denatured protein samples were loaded into 1% SDS-agarose gel, which is run at 30 mA constant current for 3.5 hours. The agarose gel was fixed in 50% methanol,12% glacial acetic acid, and 5% w/v glycerol for 1 hour and then dried overnight at 37°C. The dried gel was scanned by the silver staining method. Full details have been discussed in a previous published report [64, 65].

### RNA preparation and RNA-Seq

Total RNA was extracted from left ventricles of male mice at the age of two months (n=3) using TRIzol Reagent (Life Technologies, Thermo Fisher Scientific, Waltham, MA) according to the manufacturer's protocol. DNase I (#D9905K, Lucigen, Middleton, WI) treatment was applied to clean up genomic DNA before RNA-seq. The quantity and quality were determined by Nanodrop One (Thermo Fisher Scientific, Waltham, MA) and electrophoresis. The RNA-seq procedure was performed at the core facility of University of Wisconsin-Madison. A quality check of the raw sequencing data was performed using FastQC software [66]. Low quality reads and adapter sequences were trimmed using Trimmomatic [67]. Trimmed reads were then aligned to the mouse reference genome (NCBI *Mus musculus* GRCm39) using STAR [68]. The full dataset was uploaded to NCBI database (GSE180216, https://www.ncbi.nlm.nih.gov/geo/query/acc.cgi?acc=GSE180216)

### Differential expression and alternative splicing analyses

For gene-level expression, gene counts were estimated using "--quantMode GeneCounts" option in STAR [68]. The R package edgeR [69] was used to normalize gene counting based on trimmed mean of M-values (TMM) method [70]. Only expressed genes with at least 15 counts in more than three samples were evaluated, resulting in 14,648 genes for further analysis. Differential expression analysis were carried out for all three pairwise comparisons between WT vs. HT, WT vs. HM, HT vs. HM (three samples per group) based on negative binomial generalized linear model using edgeR package [69]. The statistical tests were corrected for multiple testing and only genes with a false discovery rate (FDR) less than 0.05 were considered significant [71]. Heatmaps were plotted using 'qplots' R package [72] and gene networks were generated using Cytoscape [73].

Alternative splicing analysis was performed for the three pairwise comparisons, i.e. WT vs. HT, WT vs. HM, and HT vs. WT, using Multivariate Analysis of Transcript Splicing software for replicates, rMATS [74]. Five types of alternative splicing events were analyzed, including skipped exon (SE), alternative 5' splice site (A5SS), alternative 3' splice site (A3SS), mutually exclusive exons (MXE), and retained intron (RI). The output from rMATS was filtered using FDR ≤ 0.05 and absolute value of ΔPSI ≥ 10% as the cut-off criterion to identify significant alternative splicing events. Splicing gene figures were generated based on 'plotGenes' function from the 'Sushi' R package functions [75].

### Gene functional annotation

Functional enrichment analysis using differential expressed and spliced genes were performed using g:Profiler [76], separately, based on Gene Ontology (Biological Process, Molecular Function, and Cellular Component), KEGG pathways and Human Phenotype Ontology (HPO). Only enriched terms with FDR more than 5% were considered significant.

### Reverse transcription and quantitative real-time PCR for RNA-Seq validation

The cDNA was synthesized by iScript™ Reverse Transcription Supermix (#1708841, Bio-Rad, Hercules, CA) according to the manufacturer's protocol. Real-time PCR was performed in a 10ul reaction, 384-well format and SsoAdvanced™ Universal SYBR® Green Supermix (#1725272, Bio-Rad). The reaction was incubated in a CFX384™ Real-time system (Bio-Rad) for polymerase activation at 95°C for 2 min, and then 40 cycles consisting of denaturation at 95°C for 15 s and annealing/extension at 60°C for 30 s; finally, the melt curve analysis was performed as default. Five samples were measured in each experimental group in duplicate, with a minimum of two independent experiments using primers listed in Table S1. The relative amount of target mRNA normalized to GAPDH was calculated according to the $2^{-\Delta\Delta Ct}$ method [77].

**Motif analysis—**Intronic coordinates for all annotated isoforms from alternatively spliced genes were extracted using R's "GenomicFeatures" package [78]. Intronic sequences were retrieved from a database generated with "BSgenome" (genome version GRCm39/NCBI) [79]. All transcript isoforms containing alternatively spliced exons were extracted by matching exon coordinates. Exon positions were used to determine the closest upstream- and downstream introns. Positions of "TCTT" motifs were determined by pattern matching and the number of matches was counted separately for each intron. Genes encoding at least one isoform with "TCTT" introns were counted as potentially regulated by RBM20.

### Statistical Analysis

GraphPad Prism software was used for statistical analysis. Results were expressed as means ± SEM. Statistical significance between groups was determined using one way ANOVA with Tukey's multiple comparisons test, or Two-way ANOVA. A nested t-test was used for intact cardiomyocyte experiments. The significance levels were $*P \leq 0.05$, $**P \leq 0.01$, $***P \leq 0.001$, $****P \leq 0.0001$.

## Supplementary Material

Refer to Web version on PubMed Central for supplementary material.

## Acknowledgements

We would like to thank our lab manager Joan Parrish for her assistance for this project and the RNA Sequencing Core Facility at University of Wisconsin-Madison for helping produce RNAseq data. This work was supported by the NHLBI HL148733 and R35HL144998, NICHD HD101870, AHA (19TPA34830072) and (19CDA34660099), The Wisconsin Alumni Research Foundation (AAH4884) and the University of Wisconsin Foundation (AAH5964).

## Non-standard Abbreviations and Acronyms

| | |
|---|---|
| **ANP** | atrial natriuretic peptide |
| **BNP** | brain natriuretic peptide |
| **DCM** | dilated cardiomyopathy |
| **FS** | fractional shortening |

| | |
|---|---|
| **FFI** | fura-2 fluorescence intensity |
| **RBP** | RNA binding protein |
| **RBM20** | RNA binding motif protein 20 |
| **RMA** | robust multi-array analysis |
| **RNP** | ribonucleoprotein |
| **LV** | left ventricle |
| **LVDd** | left ventricular end diastolic dimension |
| **LVDs** | left ventricular end systolic dimension |
| **LVPWd** | left ventricular end diastolic posterior wall dimension |
| **LVPWs** | left ventricular end systolic posterior wall dimension |
| **GO** | Gene Ontology |
| **SDS-VAGE** | sodium dodecyl sulfate vertical agarose gel electrophoresis |
| **WT** | wild type |
| **HT** | heterozygous mutation |
| **HM** | homozygous mutation |
| **H&E staining** | Hematoxylin and eosin staining |
| **RS domain** | arginine and serine-rich domain |
| **ED-SSLR** | end diastolic-stress sarcomere length relation |
| **ES-SSLR** | end systolic-stress sarcomere length |
| **SL** | sarcomere length |

## References

[1]. Brauch KM, Karst ML, Herron KJ, de Andrade M, Pellikka PA, Rodeheffer RJ, et al. , Mutations in ribonucleic acid binding protein gene cause familial dilated cardiomyopathy. J Am Coll Cardiol, 2009; 54: 930–41. [PubMed: 19712804]

[2]. Guo W, Schafer S, Greaser ML, Radke MH, Liss M, Govindarajan T, et al. , RBM20, a gene for hereditary cardiomyopathy, regulates titin splicing. Nat Med, 2012; 18: 766–73. [PubMed: 22466703]

[3]. Li D, Morales A, Gonzalez-Quintana J, Norton N, Siegfried JD, Hofmeyer M, et al. , Identification of novel mutations in RBM20 in patients with dilated cardiomyopathy. Clin Transl Sci, 2010; 3: 90–7. [PubMed: 20590677]

[4]. Guo W, Zhu C, Yin Z, Wang Q, Sun M, Cao H, et al. , Splicing Factor RBM20 Regulates Transcriptional Network of Titin Associated and Calcium Handling Genes in The Heart. Int J Biol Sci, 2018; 14: 369–380. [PubMed: 29725258]

[5]. Methawasin M, Hutchinson KR, Lee EJ, Smith JE 3rd, Saripalli C, Hidalgo CG, et al. , Experimentally increasing titin compliance in a novel mouse model attenuates the Frank-Starling

mechanism but has a beneficial effect on diastole. Circulation, 2014; 129: 1924–36. [PubMed: 24599837]

[6]. van den Hoogenhof MMG, Beqqali A, Amin AS, van der Made I, Aufiero S, Khan MAF, et al. , RBM20 Mutations Induce an Arrhythmogenic Dilated Cardiomyopathy Related to Disturbed Calcium Handling. Circulation, 2018; 138: 1330–1342. [PubMed: 29650543]

[7]. Khan MA, Reckman YJ, Aufiero S, van den Hoogenhof MM, van der Made I, Beqqali A, et al. , RBM20 Regulates Circular RNA Production From the Titin Gene. Circ Res, 2016; 119: 996–1003. [PubMed: 27531932]

[8]. Wei Guo CZ, Yin Zhiyong, Zhang Yanghai, Wang Chunyan, Walk Andrea Sanchez, Lin Ying-Hsi, McKinsey Timothy A., Woulfe Kathleen C., Ren Jun, and Chew Herbert G. Jr., The Ryanodine Receptor Stabilizer S107 Ameliorates Contractility of Adult Rbm20 Knockout Rat Cardiomyocytes. Physiological Reports, 2021.

[9]. Schneider JW, Oommen S, Qureshi MY, Goetsch SC, Pease DR, Sundsbak RS, et al. , Dysregulated ribonucleoprotein granules promote cardiomyopathy in RBM20 gene-edited pigs. Nat Med, 2020; 26: 1788–1800. [PubMed: 33188278]

[10]. Ihara K, Sasano T, Hiraoka Y, Togo-Ohno M, Soejima Y, Sawabe M, et al. , A missense mutation in the RSRSP stretch of Rbm20 causes dilated cardiomyopathy and atrial fibrillation in mice. Sci Rep, 2020; 10: 17894. [PubMed: 33110103]

[11]. Robyns T, Willems R, Van Cleemput J, Jhangiani S, Muzny D, Gibbs R, et al. , Whole exome sequencing in a large pedigree with DCM identifies a novel mutation in RBM20. Acta Cardiol, 2020; 75: 748–753. [PubMed: 31583969]

[12]. Wells QS, Becker JR, Su YR, Mosley JD, Weeke P, D'Aoust L, et al. , Whole exome sequencing identifies a causal RBM20 mutation in a large pedigree with familial dilated cardiomyopathy. Circ Cardiovasc Genet, 2013; 6: 317–26. [PubMed: 23861363]

[13]. Beqqali A, Bollen IA, Rasmussen TB, van den Hoogenhof MM, van Deutekom HW, Schafer S, et al. , A mutation in the glutamate-rich region of RNA-binding motif protein 20 causes dilated cardiomyopathy through missplicing of titin and impaired Frank-Starling mechanism. Cardiovasc Res, 2016; 112: 452–63. [PubMed: 27496873]

[14]. Refaat MM, Lubitz SA, Makino S, Islam Z, Frangiskakis JM, Mehdi H, et al. , Genetic variation in the alternative splicing regulator RBM20 is associated with dilated cardiomyopathy. Heart Rhythm, 2012; 9: 390–6. [PubMed: 22004663]

[15]. Parikh VN, Caleshu C, Reuter C, Lazzeroni LC, Ingles J, Garcia J, et al. , Regional Variation in RBM20 Causes a Highly Penetrant Arrhythmogenic Cardiomyopathy. Circ Heart Fail, 2019; 12: e005371. [PubMed: 30871351]

[16]. Pantou MP, Gourzi P, Gkouziouta A, Tsiapras D, Zygouri C, Constantoulakis P, et al. , Phenotypic Heterogeneity within Members of a Family Carrying the Same RBM20 Mutation R634W. Cardiology, 2018; 141: 150–155. [PubMed: 30557877]

[17]. Hey TM, Rasmussen TB, Madsen T, Aagaard MM, Harbo M, Molgaard H, et al. , Pathogenic RBM20-Variants Are Associated With a Severe Disease Expression in Male Patients With Dilated Cardiomyopathy. Circ Heart Fail, 2019; 12: e005700. [PubMed: 30871348]

[18]. Ling SSM, Chen YT, Wang J, Richards AM, and Liew OW, Ankyrin Repeat Domain 1 Protein: A Functionally Pleiotropic Protein with Cardiac Biomarker Potential. Int J Mol Sci, 2017; 18.

[19]. Piroddi N, Pesce P, Scellini B, Manzini S, Ganzetti GS, Badi I, et al. , Myocardial overexpression of ANKRD1 causes sinus venosus defects and progressive diastolic dysfunction. Cardiovasc Res, 2020; 116: 1458–1472. [PubMed: 31688894]

[20]. Moulik M, Vatta M, Witt SH, Arola AM, Murphy RT, McKenna WJ, et al. , ANKRD1, the gene encoding cardiac ankyrin repeat protein, is a novel dilated cardiomyopathy gene. J Am Coll Cardiol, 2009; 54: 325–33. [PubMed: 19608030]

[21]. Gravning J, Ahmed MS, von Lueder T G, Edvardsen T, and Attramadal H, CCN2/CTGF attenuates myocardial hypertrophy and cardiac dysfunction upon chronic pressure-overload. Int J Cardiol, 2013; 168: 2049–56. [PubMed: 23452880]

[22]. Bergestuen DS, Gravning J, Haugaa KH, Sahakyan LG, Aakhus S, Thiis-Evensen E, et al. , Plasma CCN2/connective tissue growth factor is associated with right ventricular dysfunction in patients with neuroendocrine tumors. BMC Cancer, 2010; 10: 6. [PubMed: 20053285]

[23]. El-Baz FK, Aly HF, and Abd-Alla HI, The ameliorating effect of carotenoid rich fraction extracted from Dunaliella salina microalga against inflammation- associated cardiac dysfunction in obese rats. Toxicol Rep, 2020; 7: 118–124. [PubMed: 31938688]

[24]. Mahmut A, Boulanger MC, Bouchareb R, Hadji F, and Mathieu P, Adenosine derived from ecto-nucleotidases in calcific aortic valve disease promotes mineralization through A2a adenosine receptor. Cardiovasc Res, 2015; 106: 109–20. [PubMed: 25644539]

[25]. Abraityte A, Lunde IG, Askevold ET, Michelsen AE, Christensen G, Aukrust P, et al. , Wnt5a is associated with right ventricular dysfunction and adverse outcome in dilated cardiomyopathy. Sci Rep, 2017; 7: 3490. [PubMed: 28615692]

[26]. Landstrom AP, Dobrev D, and Wehrens XHT, Calcium Signaling and Cardiac Arrhythmias. Circ Res, 2017; 120: 1969–1993. [PubMed: 28596175]

[27]. Zografos TA and Katritsis DG, Natriuretic Peptides as Predictors of Atrial Fibrillation Recurrences Following Electrical Cardioversion. Arrhythm Electrophysiol Rev, 2013; 2: 109–14. [PubMed: 26835050]

[28]. Nedelsky NB and Taylor JP, Bridging biophysics and neurology: aberrant phase transitions in neurodegenerative disease. Nat Rev Neurol, 2019; 15: 272–286. [PubMed: 30890779]

[29]. Shin Y and Brangwynne CP, Liquid phase condensation in cell physiology and disease. Science, 2017; 357.

[30]. Matheny T, Van Treeck B, Huynh TN, and Parker R, RNA partitioning into stress granules is based on the summation of multiple interactions. RNA, 2021; 27: 174–189. [PubMed: 33199441]

[31]. Tauber D, Tauber G, and Parker R, Mechanisms and Regulation of RNA Condensation in RNP Granule Formation. Trends Biochem Sci, 2020; 45: 764–778. [PubMed: 32475683]

[32]. Jain S, Wheeler JR, Walters RW, Agrawal A, Barsic A, and Parker R, ATPase-Modulated Stress Granules Contain a Diverse Proteome and Substructure. Cell, 2016; 164: 487–98. [PubMed: 26777405]

[33]. Markmiller S, Soltanieh S, Server KL, Mak R, Jin W, Fang MY, et al. , Context-Dependent and Disease-Specific Diversity in Protein Interactions within Stress Granules. Cell, 2018; 172: 590–604 e13. [PubMed: 29373831]

[34]. Youn JY, Dunham WH, Hong SJ, Knight JDR, Bashkurov M, Chen GI, et al. , High-Density Proximity Mapping Reveals the Subcellular Organization of mRNA-Associated Granules and Bodies. Mol Cell, 2018; 69: 517–532 e11. [PubMed: 29395067]

[35]. Marmor-Kollet H, Siany A, Kedersha N, Knafo N, Rivkin N, Danino YM, et al. , Spatiotemporal Proteomic Analysis of Stress Granule Disassembly Using APEX Reveals Regulation by SUMOylation and Links to ALS Pathogenesis. Mol Cell, 2020; 80: 876–891 e6. [PubMed: 33217318]

[36]. Hubstenberger A, Courel M, Benard M, Souquere S, Ernoult-Lange M, Chouaib R, et al. , P-Body Purification Reveals the Condensation of Repressed mRNA Regulons. Mol Cell, 2017; 68: 144–157 e5. [PubMed: 28965817]

[37]. Kedersha N, Stoecklin G, Ayodele M, Yacono P, Lykke-Andersen J, Fritzler MJ, et al. , Stress granules and processing bodies are dynamically linked sites of mRNP remodeling. J Cell Biol, 2005; 169: 871–84. [PubMed: 15967811]

[38]. Kimball SR, Horetsky RL, Ron D, Jefferson LS, and Harding HP, Mammalian stress granules represent sites of accumulation of stalled translation initiation complexes. Am J Physiol Cell Physiol, 2003; 284: C273–84. [PubMed: 12388085]

[39]. Richter JD and Sonenberg N, Regulation of cap-dependent translation by eIF4E inhibitory proteins. Nature, 2005; 433: 477–80. [PubMed: 15690031]

[40]. Ryu I and Kim YK, Translation initiation mediated by nuclear cap-binding protein complex. BMB Rep, 2017; 50: 186–193. [PubMed: 28088948]

[41]. Ayuso MI, Martinez-Alonso E, Regidor I, and Alcazar A, Stress Granule Induction after Brain Ischemia Is Independent of Eukaryotic Translation Initiation Factor (eIF) 2alpha Phosphorylation and Is Correlated with a Decrease in eIF4B and eIF4E Proteins. J Biol Chem, 2016; 291: 27252–27264. [PubMed: 27836976]

[42]. Huggins HP and Keiper BD, Regulation of Germ Cell mRNPs by eIF4E:4EIP Complexes: Multiple Mechanisms, One Goal. Front Cell Dev Biol, 2020; 8: 562. [PubMed: 32733883]

[43]. Matsumoto K, Minami M, Shinozaki F, Suzuki Y, Abe K, Zenno S, et al. , Hsp90 is involved in the formation of P-bodies and stress granules. Biochem Biophys Res Commun, 2011; 407: 720–4. [PubMed: 21439943]

[44]. Pare JM, Tahbaz N, Lopez-Orozco J, LaPointe P, Lasko P, and Hobman TC, Hsp90 regulates the function of argonaute 2 and its recruitment to stress granules and P-bodies. Mol Biol Cell, 2009; 20: 3273–84. [PubMed: 19458189]

[45]. Takasaki T, Tomimoto N, Ikehata T, Satoh R, and Sugiura R, Distinct spatiotemporal distribution of Hsp90 under high-heat and mild-heat stress conditions in fission yeast. MicroPubl Biol, 2021; 2021.

[46]. LeWinter MM and Granzier HL, Titin is a major human disease gene. Circulation, 2013; 127: 938–44. [PubMed: 23439446]

[47]. Opitz CA, Kulke M, Leake MC, Neagoe C, Hinssen H, Hajjar RJ, et al. , Damped elastic recoil of the titin spring in myofibrils of human myocardium. Proc Natl Acad Sci U S A, 2003; 100: 12688–93. [PubMed: 14563922]

[48]. Yee R, Jones DL, Jarvis E, Donner AP, and Klein GJ, Changes in pacing threshold and R wave amplitude after transvenous catheter countershock. J Am Coll Cardiol, 1984; 4: 543–9. [PubMed: 6470334]

[49]. Linke WA, Sense and stretchability: the role of titin and titin-associated proteins in myocardial stress-sensing and mechanical dysfunction. Cardiovasc Res, 2008; 77: 637–48. [PubMed: 17475230]

[50]. Granzier HL and Labeit S, The giant protein titin: a major player in myocardial mechanics, signaling, and disease. Circ Res, 2004; 94: 284–95. [PubMed: 14976139]

[51]. Methawasin M, Strom J, Borkowski T, Hourani Z, Runyan R, Smith JE 3rd, et al. , Phosphodiesterase 9a Inhibition in Mouse Models of Diastolic Dysfunction. Circ Heart Fail, 2020; 13: e006609. [PubMed: 32418479]

[52]. Tian S, Curnutte HA, and Trcek T, RNA Granules: A View from the RNA Perspective. Molecules, 2020; 25.

[53]. Gao J, Wang L, Huntley ML, Perry G, and Wang X, Pathomechanisms of TDP-43 in neurodegeneration. J Neurochem, 2018.

[54]. Polymenidou M, Lagier-Tourenne C, Hutt KR, Huelga SC, Moran J, Liang TY, et al. , Long pre-mRNA depletion and RNA missplicing contribute to neuronal vulnerability from loss of TDP-43. Nat Neurosci, 2011; 14: 459–68. [PubMed: 21358643]

[55]. Gasset-Rosa F, Lu S, Yu H, Chen C, Melamed Z, Guo L, et al. , Cytoplasmic TDP-43 De-mixing Independent of Stress Granules Drives Inhibition of Nuclear Import, Loss of Nuclear TDP-43, and Cell Death. Neuron, 2019; 102: 339–357 e7. [PubMed: 30853299]

[56]. Prasad J, Colwill K, Pawson T, and Manley JL, The protein kinase Clk/Sty directly modulates SR protein activity: both hyper- and hypophosphorylation inhibit splicing. Mol Cell Biol, 1999; 19: 6991–7000. [PubMed: 10490636]

[57]. Ding B and Sepehrimanesh M, Nucleocytoplasmic Transport: Regulatory Mechanisms and the Implications in Neurodegeneration. Int J Mol Sci, 2021; 22. [PubMed: 35008458]

[58]. Sun M, Jin Y, Zhu C, Zhang Y, Liss M, Gotthardt M, et al. , RBM20 phosphorylation on serine/arginine domain is crucial to regulate pre-mRNA splicing and protein shuttling in the heart. bioRxiv, 2020: 2020.09.15.297002.

[59]. Collins TJ, ImageJ for microscopy. Biotechniques, 2007; 43: 25–30.

[60]. Brody MJ, Feng L, Grimes AC, Hacker TA, Olson TM, Kamp TJ, et al. , LRRC10 is required to maintain cardiac function in response to pressure overload. Am J Physiol Heart Circ Physiol, 2016; 310: H269–78. [PubMed: 26608339]

[61]. O'Connell TD, Rodrigo MC, and Simpson PC, Isolation and culture of adult mouse cardiac myocytes. Methods Mol Biol, 2007; 357: 271–96. [PubMed: 17172694]

[62]. Granzier HL and Irving TC, Passive tension in cardiac muscle: contribution of collagen, titin, microtubules, and intermediate filaments. Biophys J, 1995; 68: 1027–44. [PubMed: 7756523]

[63]. Helmes M, Najafi A, Palmer BM, Breel E, Rijnveld N, Iannuzzi D, et al. , Mimicking the cardiac cycle in intact cardiomyocytes using diastolic and systolic force clamps; measuring power output. Cardiovascular Research, 2016; 111: 66–73. [PubMed: 27037258]

[64]. Warren CM, Krzesinski PR, and Greaser ML, Vertical agarose gel electrophoresis and electroblotting of high-molecular-weight proteins. Electrophoresis, 2003; 24: 1695–702. [PubMed: 12783444]

[65]. Zhu C and Guo W, Detection and quantification of the giant protein titin by SDS-agarose gel electrophoresis. MethodsX, 2017; 4: 320–327. [PubMed: 29872636]

[66]. Andrews S, FastQC: A Quality Control Tool for High Throughput Sequence Data. 2010.

[67]. Bolger AM, Lohse M, and Usadel B, Trimmomatic: a flexible trimmer for Illumina sequence data. Bioinformatics, 2014; 30: 2114–2120. [PubMed: 24695404]

[68]. Dobin A, Davis CA, Schlesinger F, Drenkow J, Zaleski C, Jha S, et al. , STAR: ultrafast universal RNA-seq aligner. Bioinformatics, 2013; 29: 15–21. [PubMed: 23104886]

[69]. Robinson MD, McCarthy DJ, and Smyth GK, edgeR: a Bioconductor package for differential expression analysis of digital gene expression data. Bioinformatics, 2010; 26: 139–140. [PubMed: 19910308]

[70]. Robinson MD and Oshlack A A scaling normalization method for differential expression analysis of RNA-seq data. Genome Biology, 2010; 11.

[71]. Benjamini Y and Hochberg Y, Controlling the False Discovery Rate - a Practical and Powerful Approach to Multiple Testing. Journal of the Royal Statistical Society Series B-Statistical Methodology, 1995; 57: 289–300.

[72]. Warnes GRBB, Bonebakker L, Gentleman R, Liaw WHA, Lumley T., gplots: various R programming tools for plotting data. R package version 3.1.1, 2020.

[73]. Shannon P, Markiel A, Ozier O, Baliga NS, Wang JT, Ramage D, et al. , Cytoscape: A software environment for integrated models of biomolecular interaction networks. Genome Research, 2003; 13: 2498–2504. [PubMed: 14597658]

[74]. Shen S, Park JW, Lu ZX, Lin L, Henry MD, Wu YN, et al. , rMATS: robust and flexible detection of differential alternative splicing from replicate RNA-Seq data. Proc Natl Acad Sci U S A, 2014; 111: E5593–601. [PubMed: 25480548]

[75]. DH P, Sushi: Tools for visualizing genomics data. R package version 1.26.0., 2020.

[76]. Raudvere U, Kolberg L, Kuzmin I, Arak T, Adler P, Peterson H, et al. , g:Profiler: a web server for functional enrichment analysis and conversions of gene lists (2019 update). Nucleic Acids Research, 2019; 47: W191–W198. [PubMed: 31066453]

[77]. Livak KJ and Schmittgen TD, Analysis of relative gene expression data using real-time quantitative PCR and the 2(-Delta Delta C(T)) Method. Methods, 2001; 25: 402–8. [PubMed: 11846609]

[78]. Lawrence M, Huber W, Pages H, Aboyoun P, Carlson M, Gentleman R, et al. , Software for computing and annotating genomic ranges. PLoS Comput Biol, 2013; 9: e1003118. [PubMed: 23950696]

[79]. H P, BSgenome: Software infrastructure for efficient representation of full genomes and their SNPs. R package version 1.62.0, 2021.

**Highlights:**

- An *RBM20* mutation S639G leads to dilated cardiomyopathy and high mortality rate.
- Mutation results in RBM20 nucleocytoplasmic transport and protein condensates.
- Protein condensates caused by RBM20 mutation are a new causative mechanism of DCM.

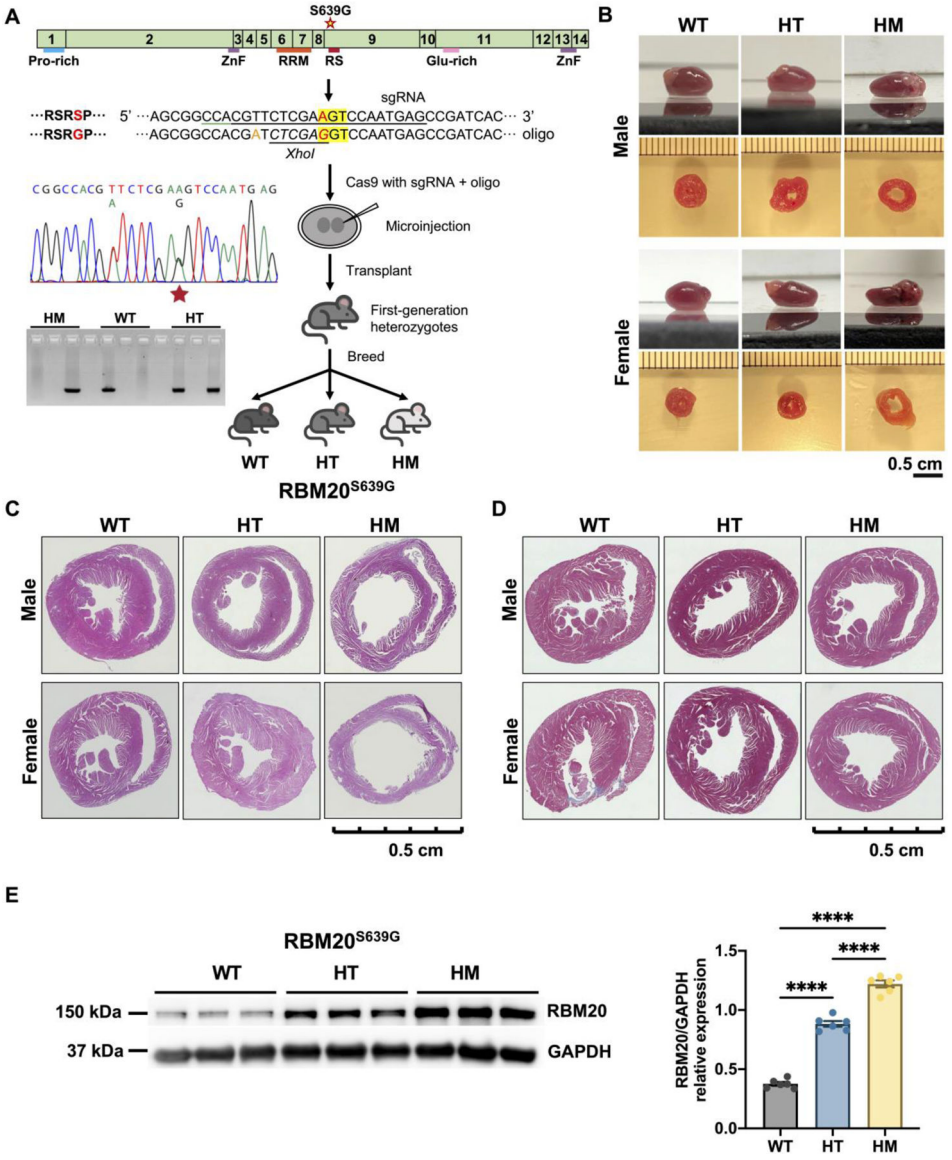


**Figure 1.** ***Rbm20*$^{S639G}$ KI mouse model, histological and gross anatomical assessments.**

**(A)** Schematic diagram of *Rbm20* gene structure and generation of a S639G mutation knock-in mouse (*Rbm20*$^{S639G}$) through CRISPR/Cas9 technology. The schematic shows the mouse *Rbm20* gene and coded protein domains. The mutation hot spot of RS domain is indicated as "RSRSP". The target amino acid is highlighted in yellow in "RSRSP", and the point mutation site is in red. The sgRNA is underlined in black and the orange nucleotides are in the silent mutation site. The desired switch from AGT (S) to GGT (G) introduced an *XhoI* restriction site and facilitated the genotyping. The edited *Rbm20* alleles in mice were confirmed by Sanger sequencing and PCR genotyping. **(B)** Gross anatomy comparing WT, HT and HM hearts in the top panels of both male and female hearts, and slice anatomy at the mid-ventricular level comparing WT, HT and HM in the bottom panels of male and female hearts (n=3, the number of animals for WT, HT, and HM of each gender, respectively). The black line at the bottom represents a 0.5 cm ruler. **(C)** Representative images of hematoxylin

and eosin staining of cross-section of mouse hearts at the age of two months in both males and females (n=3, the number of animals for WT, HT, and HM of each gender, respectively). The scale bar at the bottom indicates a 0.5 cm ruler. **(D)** Representative images of Masson's trichrome staining in both males and females. The scale bar at the bottom indicates a 0.5 cm ruler. **(E)** Western Blotting of RBM20 and quantification in WT, HT and HM. N=3, number of male animals used, duplicate of blotting were calculated. Error bars indicate mean ± SEM and statistical significance is indicated as $*P \leq 0.05$, $**P \leq 0.01$, $***P \leq 0.001$, $****P \leq 0.0001$. Tukey's multiple comparisons test was used. RRM, RNA binding motif; RS, arginine/serine; WT, wild type; HT, heterozygotes; HM, homozygotes.

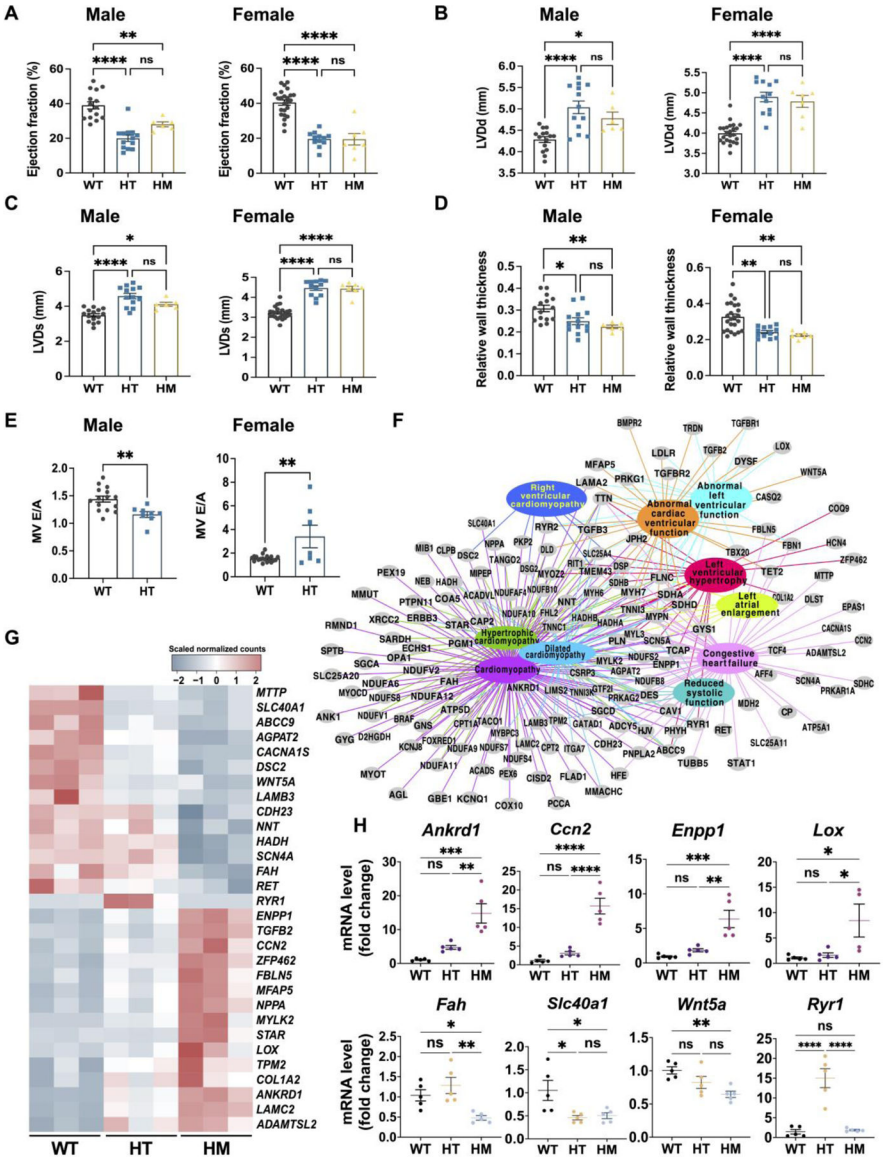


**Figure 2. *In vivo* cardiac functional assessment in *Rbm20*$^{S639G}$ mutation KI mice and transcriptomic profiling.**

**(A)-(E)** Transthoracic echocardiography was performed on WT (n=17, 10 females, 7 males), HT (n=13, 6 females, 7 males), and HM (n=13, 7 females, 6 males) mice at the age of two months. **(A)** Ejection fraction (EF). **(B)** Left ventricular diastolic diameter (LVDd). **(C)** Left ventricular systolic diameter (LVDs). **(D)** Relative wall thickness (RWT). **(E)** Mitral E/A ratio. Tukey's multiple comparisons test was used. **(F)** Networks of differentially expressed genes (between WT, HT, and HM mice) clustering in cardiomyopathy related HPO terms. **(G)** Heatmap of the 15 most up-and down- regulated genes (HM vs. WT) within the 10 HPO terms selected in **(F)**. **(H)** Validation of selected genes with quantitative real-time PCR (n=5, the number of animals). WT, wild type; HT, heterozygotes; HM, homozygotes; NS, non-significance. Error bars indicate mean ± SEM and statistical significance is indicated as $*P \leq 0.05$, $**P \leq 0.01$, $***P \leq 0.001$, $****P \leq 0.0001$. Tukey's multiple comparisons test was used.

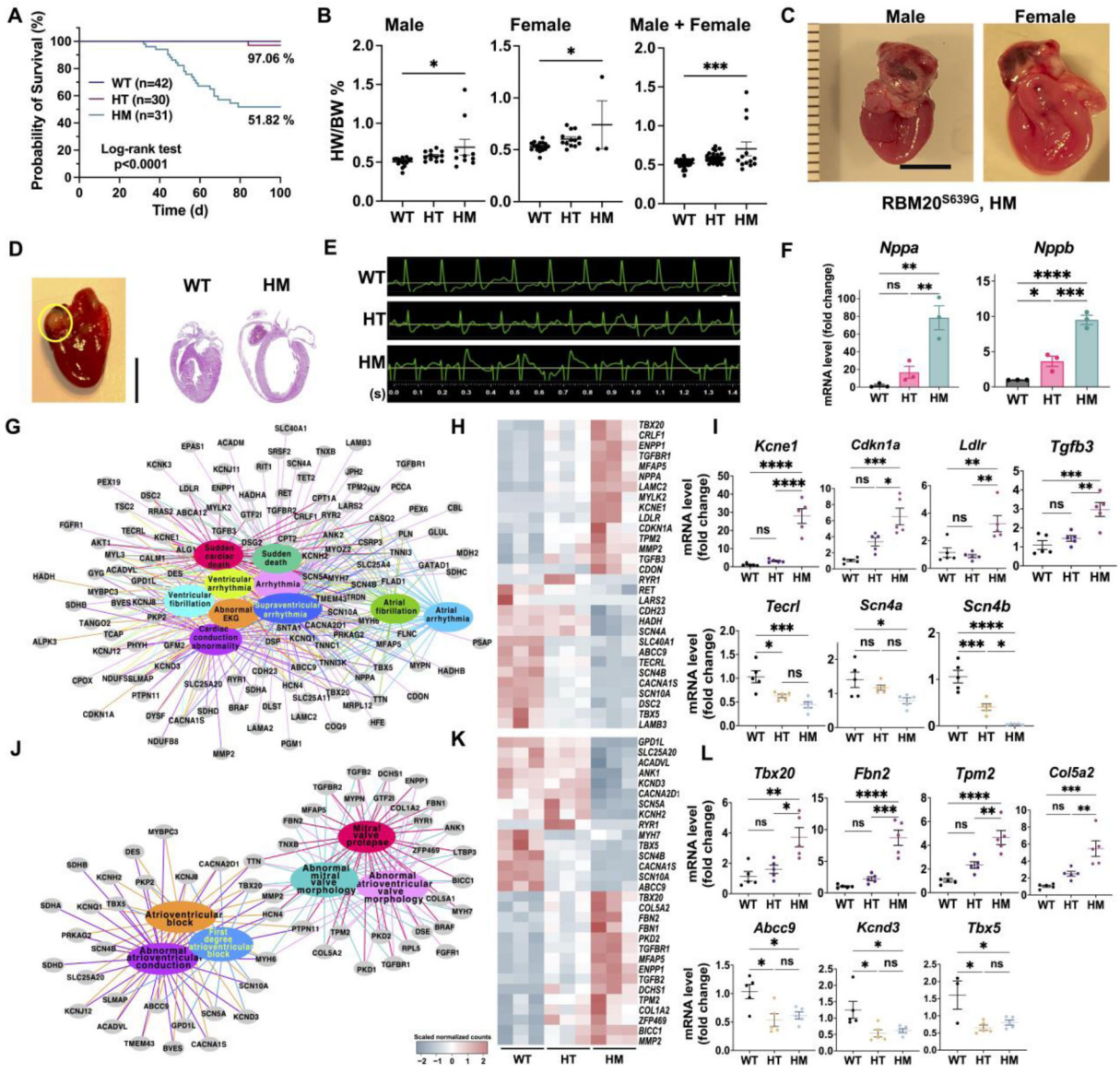


**Figure 3. Survival curve and transcriptomic profiling.**

**(A)** Kaplan–Meier survival curves of WT (n=42), HT (n=30), and HM (n=31) mice. Statistical significance was determined by log-rank (Mantel–Cox) test with two degrees of freedom (P<0.0001) (n is the number of individual littermates of each genotype). **(B)** Heart weight vs. body weight of WT (n=32, 17 females, 15 males), HT (n=25,13 females, 12 males), and HM (n=13, 3 females, 10 males) mice at the age of two months. Error bars indicate mean ± SEM and statistical significance is indicated as $*P \leq 0.05$, $**P \leq 0.01$, $***P \leq 0.001$, $****P \leq 0.0001$. Tukey's multiple comparisons test was used. **(C)** Enlarged atria were observed in HM mice at the age of two months. The scale bar at the bottom indicates a 0.5 cm ruler. **(D)** Necropsy and hematoxylin and eosin staining of heart tissue of HM mice with sudden death. A WT mouse with similar age was sacrificed for control. The scale bar at the bottom indicated a 0.5 cm ruler. **(E)** Representative ECG images from WT, HT and HM mice. **(F)** Quantitative PCR verification of the heart failure markers *Nppa* and *Nppb*

(n=3, the number of animals). Error bars indicate mean ± SEM and statistical significance is indicated as *$P \leq 0.05$, **$P \leq 0.01$, ***$P \leq 0.001$, ****$P \leq 0.0001$. Tukey's multiple comparisons test was used. **(G)** Networks of differentially expressed genes (between WT, HT, and HM mice) clustering in 10 arrhythmia related HPO terms. **(H)** Heatmap of the 15 most up- and down- regulated genes (HM vs. WT) within the 10 selected HPO terms selected in **(G)**. **(I)** Validation of selected genes with quantitative real-time PCR (n=5, the number of animals). Error bars indicate mean ± SEM and statistical significance is indicated as *$P \leq 0.05$, **$P \leq 0.01$, ***$P \leq 0.001$, ****$P \leq 0.0001$. Tukey's multiple comparisons test was used. **(J)** Networks of differentially expressed genes (between WT, HT, and HM mice) clustering in abnormal atrioventricular conduction-related HPO terms. **(K)** Heatmap of the 15 most up-and down-regulated genes (HM vs. WT) within the 6 selected HPO terms selected from **(K)**. **(L)** Validation of selected genes with quantitative real-time PCR (n=5, the number of animals). Error bars indicate mean ± SEM and statistical significance is indicated as *$P \leq 0.05$, **$P \leq 0.01$, ***$P \leq 0.001$, ****$P \leq 0.0001$. Tukey's multiple comparisons test was used. WT, wild type; HT, heterozygotes; HM, homozygotes.

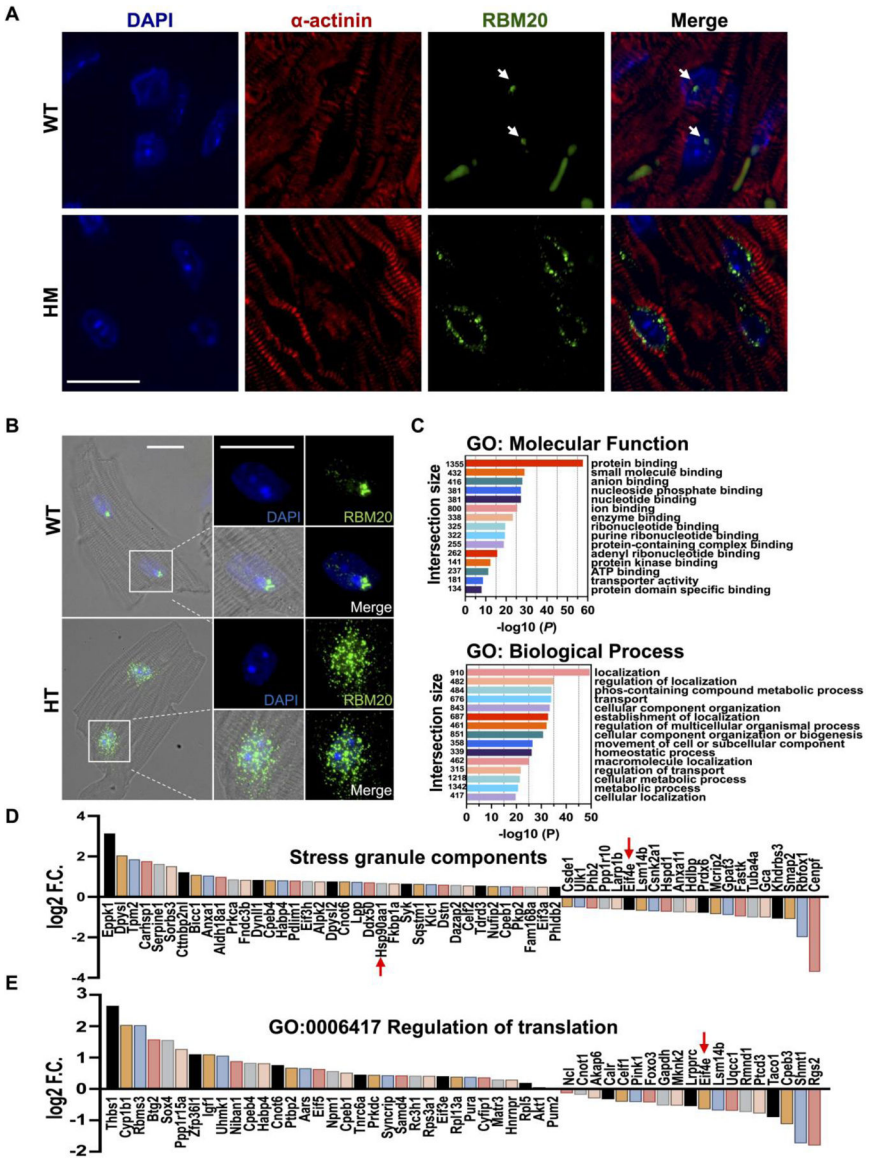


**Figure 4. RBM20 trafficking, formation of RNA-protein condensates and GO analysis.**

**(A)** Immunohistochemistry staining with paraffin section of WT and HM mouse hearts. Scale bar, 20μm. **(B)** Immunocytochemical staining of isolated WT and HT cardiomyocytes. Scale bar, 20μm. **(C)** GO enrichment analysis of DEGs (WT vs. HT vs. HM). Protein binding and localization relevant GO terms with significant *P*-values were shown. Numbers indicate the intersection size (number of differentially expressed genes) of each term. **(D)** Differentially expressed genes encoding stress granule components. Log2 fold change ≥ 0.5 and ≤ −0.5 were shown in the bar chart. **(E)** Differentially expressed genes encoding components involving translational regulation (Biological Process, term ID: 0006417). WT, wild type; HT, heterozygotes; HM, homozygotes; GO, gene ontology; F.C., fold change.

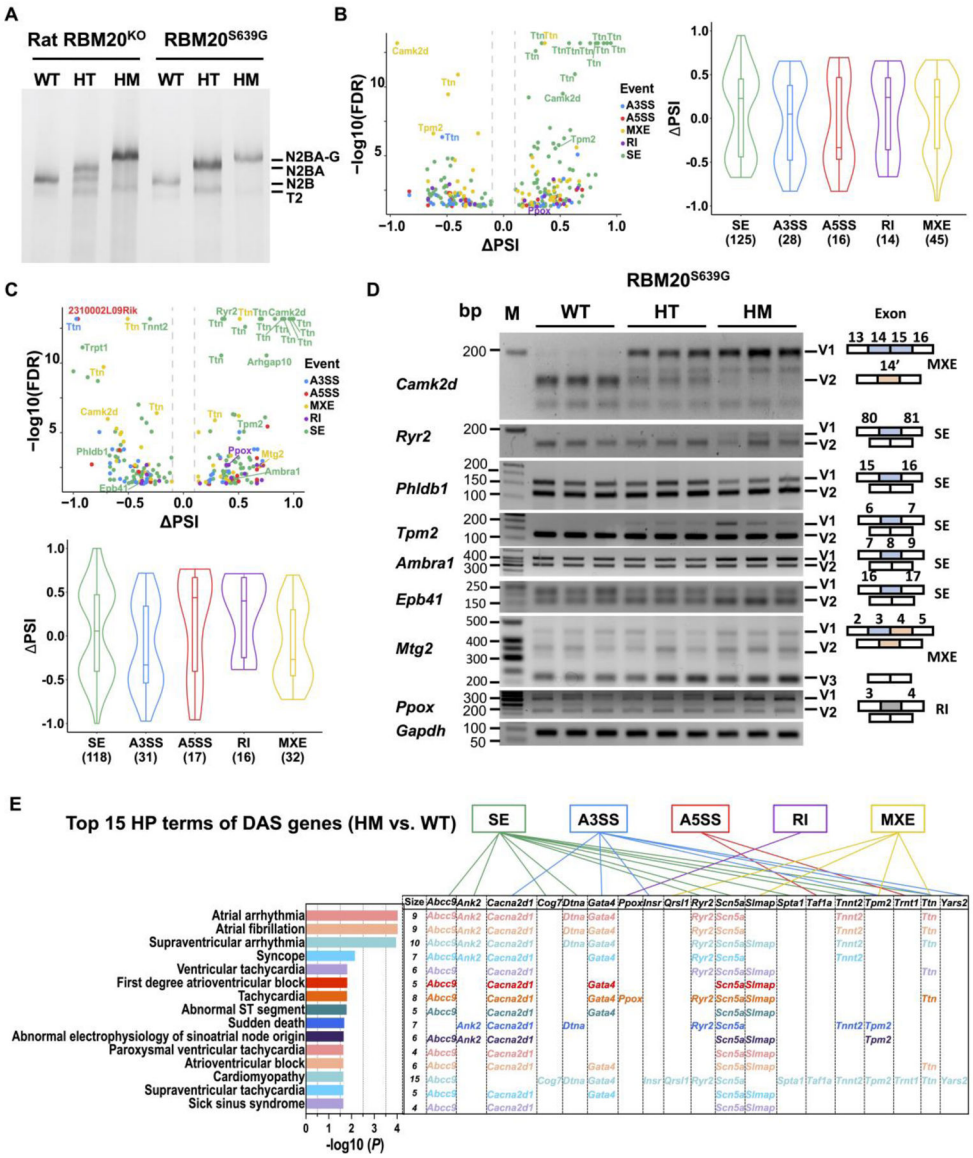


**Figure 5. Splicing variant analysis with RNA seq data and splicing events involving cardiac function.**

**(A)** Titin isoform switching resulting from alternative splicing was detected in WT, HT, and HM heart tissues through vertical sodium dodecyl sulfate (SDS)-1% agarose gel electrophoresis (VAGE) system. N2BA-G, N2BA, and N2B represent different sizes of titin isoforms. **(B)** Volcano and violin plots of splicing events of the differentially alternative spliced genes in HT hearts. **(C)** Volcano and violin plots of splicing events of the differentially alternative spliced genes in HM hearts. **(D)** Validation of selected alternative spliced genes with RT-PCR and schematic diagram of selected genes with different splicing events. **(E)** DAS genes falling into the top 15 HPO terms related to cardiac function, and splicing events of selected genes are presented. The numbers indicated the intersection size of each term. (HM vs. WT FDR ≤ 0.05). GAPDH, loading control; SE, skipped exon; A5SS, alternative 5’ splice site; A3SS, alternative 3’ splice site; MXE, mutually exclusive exons;

RI, retained intron; DAS, differentially spliced genes; WT, wild type; HT, heterozygotes; HM, homozygotes; bp, base pair; V, variant; T2, degraded titin.

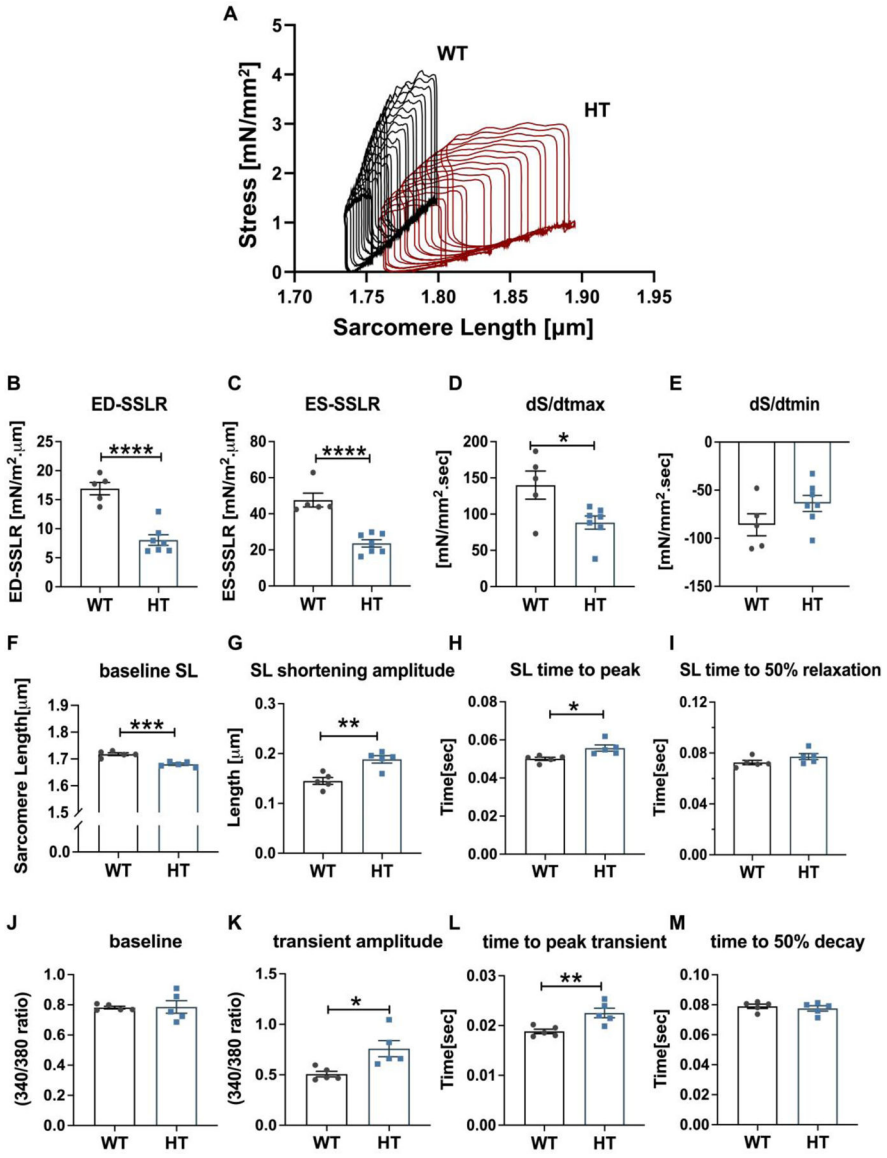


**Figure 6. Cardiomyocyte diastolic stiffness, contractility and calcium transient.**

Cardiomyocytes were stimulated at 4 Hz in the solutions at physiological temperature (37° C). (**A)-(E)** Loaded intact myocyte force measurement. WT, n= 5; HT, n= 7 mice, and 4–10 cells per mouse. **(A)** Representative examples of work loop series of WT and HT cells. **(B)** The slope of ED-SSLR, reflecting cellular diastolic stiffness. **(C)** The slope of ES-SSLR, reflecting cellular contractility. **(D)** The maximal rate of stress rises during isometric contraction. **(E)** The maximal rate of stress decline. (**F)-(I)** Unloaded intact myocyte SL shortening-relengthening. n= 5 mice, and ~50 cells per mouse. **(F)** The diastolic (baseline) sarcomere length of WT and HT cardiomyocytes. **(G)** The shortening amplitude of WT and HT cardiomyocytes. **(H)** The time to peak shortening. **(I)** The time from peak to 50% baseline. (**J)-(M)** Unloaded intact myocyte $Ca^{2+}$ release-reuptake. $Ca^{2+}$ transient of isolated intact cardiomyocytes was measured with Fura-2 340/380 signal. (n= 5 mice, and ~50 cells per mouse). **(J)** Diastolic baseline signal. **(K)** The transient amplitude. **(L)** The

time to peak transient. **(M)** The time from peak to 50% transient decay. WT, wild type; HT, heterozygotes; ED-SSLR, end diastolic-stress sarcomere length relation; ES-SSLR end systolic-stress sarcomere length; SL, sarcomere length. Error bars indicate mean ± SEM and statistical significance is indicated as $*P \leq 0.05$, $**P \leq 0.01$, $***P \leq 0.001$, $****P \leq 0.0001$. Nested t-test was used.